J Seismol (2009) 13:73–87
DOI 10.1007/s10950-008-9116-0

ORIGINAL ARTICLE

Seasonal variations of cross correlations of seismic noise in Israel

N. Kraeva · V. Pinsky · A. Hofstetter

Received: 4 February 2008 / Accepted: 24 June 2008 / Published online: 24 July 2008
© Springer Science + Business Media B.V. 2008

Abstract The long-period microseismic noise was recently found to carry deterministic information about the crust and upper mantle structure in the cross-section between the two station sites in terms of the surface wave Green function, which is theoretically proportional to the noise cross-correlation function (NCF) for the long-term observations at the pair of the BB stations. We performed daily-long cross correlations for the period of 2–3 years between the 7 BB stations, distributed in the Eastern Mediterranean, and stacked them for every month of a year. A preprocessing of the broadband waveforms included whitening of the direct and inverse DFT of the waveforms to avoid influence of earthquakes recordings and to equalize energy of different types of microseisms. As the result, we have found that the NCFs obtained exhibit clear seasonal variations within period band 2–20 s persistent from year to year. For the best description of these variations, we applied seasonal diagrams, which presented the distribution of the NCF maximal amplitudes in three narrow frequency bands, with respect to the month of a year. The diagrams helped in determining that these variations can be split into four types. The different types of the seasonal NCF variations are assumed to be attributed to the four certain remote deep ocean regions, which are responsible for the increased microseismic activity due to the specific interaction between the ocean waves and the bottom during ocean storms.

N. Kraeva (✉)
University of Western Ontario, London,
Ontario, Canada
e-mail: nadezdakraeva@aol.com

V. Pinsky · A. Hofstetter
Geophysical Institute of Israel, Lod, Israel

Keywords Cross-correlation function · Microseismic noise · Broadband recordings · Sources of microseismic noise

1 Introduction

The cross-correlation process applied to long broadband microseism recordings accumulates over time the coherent deterministic constituent of the ambient noise propagating through the station pair under consideration in the direction given by the station pair azimuth. This non-trivial result was proved theoretically for a homogeneous medium with attenuation (Snieder 2004) and for a general case of inhomogeneous medium (Wapenaar 2004).

Shapiro and Campillo (2004) and Shapiro et al. (2005) have demonstrated that the waveform emerging from stacking noise cross-correlation functions (NCFs) for vertical–vertical BB seismometers coincides with an accuracy of a scaling factor with an actual Rayleigh wave Green function of the trace between the receivers and saves its real spectral-time structure. Broadband dispersion curves extracted from this data form a database for generating one-dimensional shear velocity profiles between pairs of stations and two-dimensional group velocity maps using a network of BB stations, with essentially improved resolution if compared to traditional source-station methods (Shapiro and Campillo 2004; Paul et al. 2005; Sabra et al. 2005a, b; Shapiro et al. 2005; Weaver 2005; and many others).

With a motivation of optimization of the noise-based seismic tomography, attempts of better understanding of seismic noise behavior and origin have been made recently. Using ocean stations data, it was shown that ambient noise is composed of two components: long-distance coherent wavefield and locally generated noise, which obscures observations of the first one (Lin et al. 2006). The upper bound of the long-distance coherent noise component level may be probably estimated from the Peterson's standard low noise model (Peterson 1993). The longest distance at which a high signal-to-noise ratio (SNR) cross-correlation signal is observed is determined as a noise coherence distance. Scattering and inelastic attenuation decrease this distance, more strongly at the shorter period end of the spectrum.

To the first order for a weakly scattering medium, the areas of constructive interference for the noise sources giving basic contribution to the NCFs are located in the two broad end-fire beams (Snieder 2004; Sabra et al. 2005b). Because, in reality, the sources of ambient noise are not uniformly distributed either in space, or in time (Rhie and Romanowicz 2006), the NCF is not a symmetric function with respect to the arrival time. The amplitudes of causal and anticausal its parts are not equal; moreover, they might change independently of one another, subject to the season and the station pair orientation (Stehly et al. 2006).

Ambient seismic noise is mostly composed of surface waves originated close to the surface of the Earth apparently due to pressure perturbations, mainly in oceans. The point of a scientific debate is where the microseism noise is originated, in deep water or near coastlines. Thus, Stehly et al. (2006), on the base of year-long cross-correlation study of broadband ambient noise observed worldwide, found a surprising fact that primary and secondary microseisms observed locally have different regions of origin and different seasonal behavior. According to their study, while at periods between 5 and 10 s (secondary microseism), most of the coherence noise is coming from the coast and remains stable during the whole year, the noise at periods between 10 and 20 s (primary microseism) has a strong seasonal variability and is clearly related to ocean wave activity in deep water. Because primary and secondary microseisms have periods similar to the main sea swell period and half period, respectively, they are related probably to the interaction of the sea waves with the sea bottom and coast (Longuet-Higgins 1950; Gutenberg 1951; Stehly et al. 2006). The new paper of Kedar et al. (2008) reports the first application of the Longuet-Higgins (1950) theory to a real data in a form of wave spectra and proves that a significant part of the microseism energy originates in the open ocean due to acoustic resonance, provided by the wave-to-wave interaction over the bottom at specific depths range.

On the other hand, Rhie and Romanowicz (2006) investigated the relation between the strong ocean storm in the North Pacific and the Earth's hum in the frequency range 2–7 mHz basing on the observations performed on seismic arrays in Japan and California during 4 days without strong earthquakes. They inferred that the hum events occur close to the shore rather than the deep ocean, so that ocean wave energy is coupled with the solid earth predominantly near coastlines. They have found also that during the winter periods in the Northern Hemisphere, there is a strong correlation between variation in seismic amplitude at long- (∼240 s) and short-period bands (2–25 s) that can indicate that the microseisms and the hum events have a common generation mechanism. Preliminary results of study of azimuthal distribution of strong ambient noise sources made by Yang and Ritzwoller (2008) support this conclusion and show that both primary and secondary microseisms recorded at numerical stations worldwide come dominantly from the direction of nearly coastlines.

In our research, using 2–3-year data of small broadband network operating in Israel, we have found main types of seasonal variations of NCFs in different frequency bands, reflecting the relative annual regularity of changes of activity of the long-distance coherent seismic noise. Thus, we get the additional detailed and informative indication for identification of the long-distance microseism source regions.

2 Data processing

We use vertical broadband 24-h-long seismograms recorded in 2001–2005 by six stations of the Israel Seismograph Network (EIL, HRFI, KZIT, AMZI, MMLI, and KSDI) and Cyprus station CSS (Fig. 1). Table 1 lists all possible pair combinations of these seven stations and their assigned numbers and also distances between them and azimuths of great circles passing through these pairs (named here simply as azimuths). The order of names in every station pair corresponds to the cross-correlation order; station pairs with opposite order have opposite numbers in Table 1. Their cross correlations are equivalent but have the reverse order of points so that causal (positive time delay) and anticausal (negative time delay) parts switch places. Pairs of stations are divided into four groups; the reason of this division will be explained later. The pair of stations EIL-HRFI located too close (41 km) to each other is not included in this table. Distances between stations in other pairs vary in the range 86–606 km that decrease surface wave resolution of our network as a whole by periods about 20–30 s (while the most distant separated pairs of our stations can resolve longer periods).

The waveform processing is carried out on 24-h time bases using SAC utilities. After decimation to 2.5 samples per second ($\Delta t = 0.4$ s), instrument correction, and band-pass filtering in the period band from 2 to 80 s, we apply the procedure for temporal and spectral normalization developed by Bensen et al. (2007) and Yang et al. (2007). For time-domain normalization, we calculate the envelope of a seismogram in the sub-band 15–50 s smoothed over a 40-s moving window and use the inverse of this envelope for weighting of

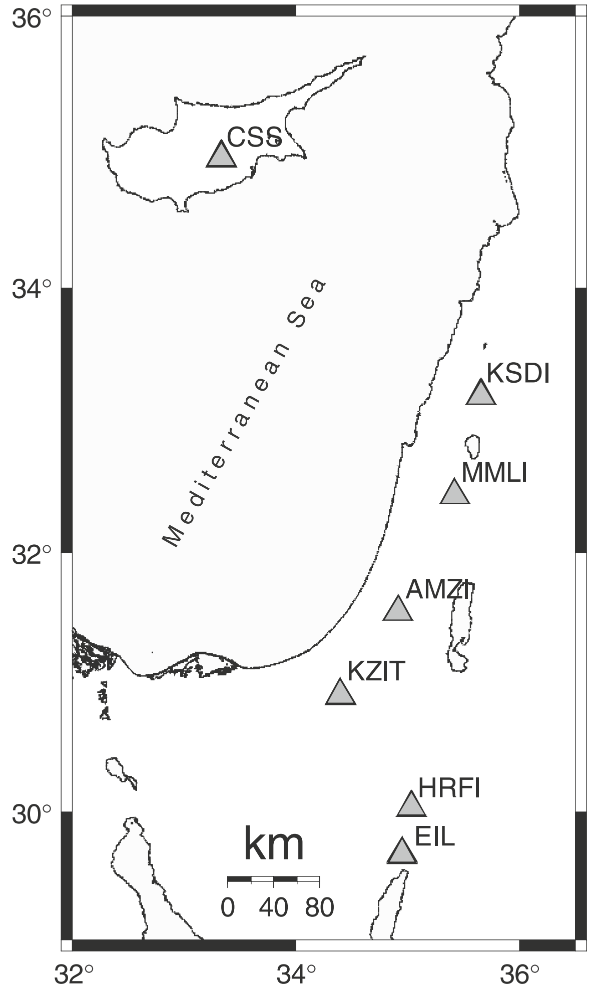

Fig. 1 Israeli broadband seismic network plus CSS broadband station of Cyprus

the original daily time-series (Bensen et al. 2007 name it running-absolute-mean normalization). This procedure suppresses temporally localized events such as earthquakes and instrument irregularities. Insufficiently suppressed earthquake signals appear on cross correlations as spurious small-time precursory arrivals spreading with high velocities and outstripping surface waves, concentrating manly in the vicinity of cross-correlation zero time. Bensen et al. (2007) have tested some other normalization techniques including one-bit one used by Stehly et al. (2006) and found that these two methods give very similar results, but the running-absolute-mean method provides a small enhancement to SNR values above one-bit

Table 1 Four groups of broadband seismic station pairs in Israel with different types of seasonal variations of their long-distance coherent noise

No.	Station pair	Distance (km)	Azimuth (degrees)
NE type ($8^\circ \le az \le 34^\circ$)			
1	MMLI-EIL	310	8
2	KSDI-HRFI	355	9
3	KSDI-EIL	396	10
4	KSDI-MMLI	87	15
5	KSDI-AMZI	195	21
6	KSDI-KZIT	280	25
7	MMLI-AMZI	110	26
8	MMLI-KZIT	196	30
9	AMZI-KZIT	86	34
NW type ($az < 8^\circ$; $az \ge 313^\circ$)			
10	MMLI-HRFI	269	7
11	AMZI-EIL	208	359
12	AMZI-HRFI	168	356
13	CSS-KZIT	461	348
14	CSS-EIL	606	346
15	CSS-HRFI	569	344
16	KZIT-EIL	147	339
17	CSS-AMZI	406	339
18	KZIT-HRFI	114	328
19	CSS-MMLI	340	326
20	CSS-KSDI	291	313
SE type ($132^\circ \le az \le 167^\circ$)			
−20	KSDI-CSS	291	132
−19	MMLI-CSS	340	145
−18	HRFI-KZIT	114	147
−17	AMZI-CSS	406	158
−16	EIL-KZIT	396	159
−15	HRFI-CSS	569	163
−14	EIL-CSS	606	165
−13	KZIT-CSS	461	167
SW type ($176^\circ \le az \le 215^\circ$)			
−12	HRFI-AMZI	168	176
−11	EIL-AMZI	208	179
−10	HRFI-MMLI	269	188
−1	EIL-MMLI	310	188
−2	HRFI-KSDI	355	190
−3	EIL-KSDI	396	190
−4	MMLI-KSDI	87	195
−5	AMZI-KSDI	195	201
−6	KZIT-KSDI	280	205
−7	AMZI-MMLI	110	206
−8	KZIT-MMLI	196	210
−9	KZIT-AMZI	86	215

The order of names in every station pair corresponds to the cross-correlation order; station pairs with opposite order are assigned opposite numbers.

normalization at all periods and is more flexible and adaptable to the data.

Spectral normalization means inverse weighting of the amplitude spectrum by its smoothed form. Such spectral whitening puts all spectral components of the seismic noise in equal status, decreasing its most energetic amplitude peaks, first of all, corresponding to the widespread secondary microseisms, and increasing the weaker spectral components, thereby broadening the band of the ambient noise cross-correlation signal.

We perform broadband daily-long cross correlations between stations and stack them for every month of a year and for all observation periods. Two examples of cross correlations of noise recorded by stations AMZI and HRFI and CSS and EIL, stacked for 2.2 and 3.3 years, respectively, are shown in Fig. 2. The waveform emerging from the summary cross-correlation in the group velocity window 1.5–4.5 km/s is Rayleigh wave Green function and will be considered here as a signal. The clear normal dispersion of this Rayleigh wave is observed, with the longer periods arriving earlier. For stations AMZI and HRFI (Fig. 2a), the amplitude of a signal observed in the anticausal part of the cross correlation strongly exceeds that of the causal part in the period sub-bands of 5–10 and 10–20 s, implying probably that at these periods, the coherent noise energy flux from HRFI to AMZI (south to north) is several times greater than the opposite one. On the contrary, at short periods 2–5 s, the energy flux might have a prevalent opposite direction. On the other side, the summary cross-correlation at longer periods (20–30 s) is only slightly asymmetric. To generalize, such pattern of amplitude asymmetry, with some variations, is typical for cross correlations corresponding to the continental traces in Israel.

Resolution of cross correlations evaluated by SNR is being improved with increasing of duration of observations (Bensen et al. 2007), but even for 3-year data, the resolution of mixed marine-continental traces passed through the Cypriot island station CSS remains essentially worse in comparison with continental ones so that their NCFs are bounded by the periods T = 10–30 s (Fig. 2b). At short periods in the sub-bands 2–5 and 5–10 s for these traces, we never observe the

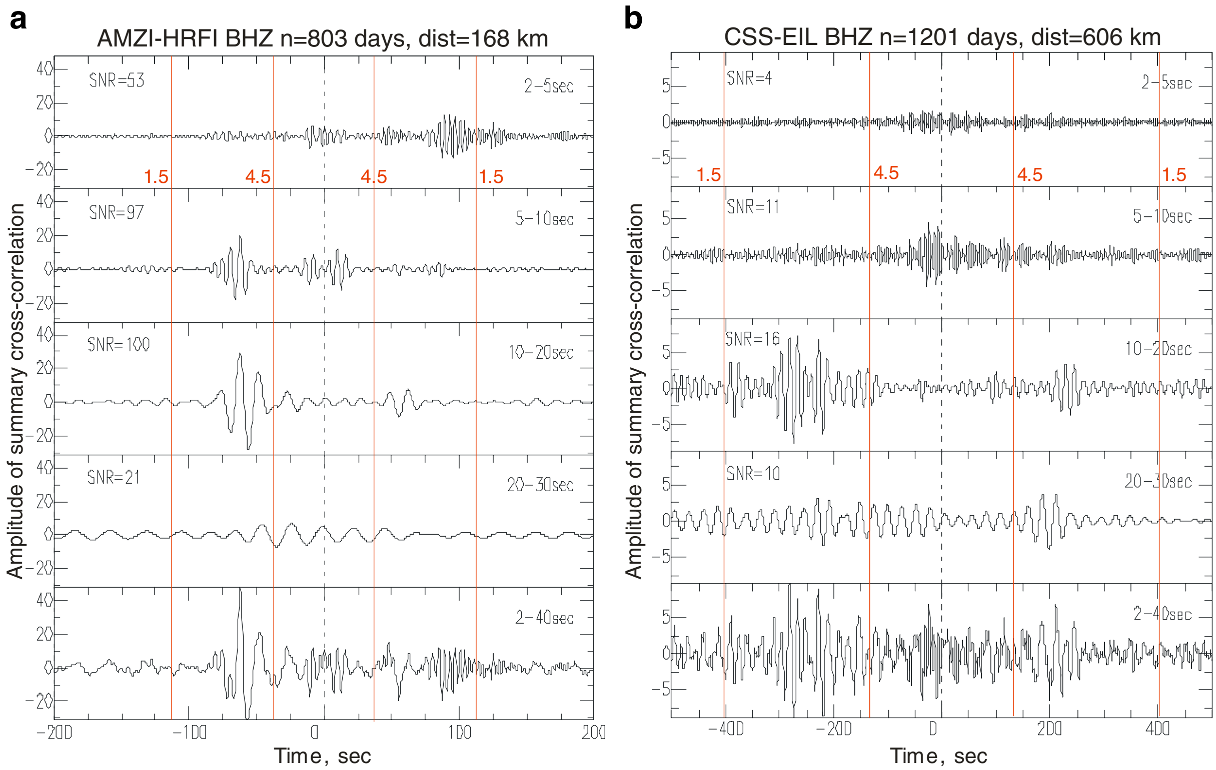

Fig. 2 Two examples of vertical–vertical cross-correlations of ambient noise recorded in 2002–2005 by stations AMZI and HRFI (**a**) and CSS and EIL (**b**), stacked for 2.2 and 3.3 years, accordingly. The successively longer period passbands are presented in the *first four panels* of the figure, and the whole broadband cross-correlation (2–40-s passband) is shown at *bottom*. The clear normal dispersion of the Rayleigh wave is observed. *Vertical red solid lines* indicate the signal windows corresponding to group velocities between 1.5 and 4.5 km/s. SNR defined in each band as the ratio of signal to trailing at large cross-correlation time noise is indicated *leftward* in panels. The interstation distance is 168 km for the pair AMZI and HRFI and 606 km for the pair CSS and EIL

expected Green function pattern but a very noisy cross-correlations wavelet instead. This supports the conclusion made by Lin et al. (2006) that island stations suffer from locally generated noise, which is incoherent with noise at distant continental stations and, therefore, obscures the observation of the long-distance coherent wavefield. The local incoherent noise at island stations is most probably originated from the effects of nearby sea wave activity. Multipathing effect as a result of strong horizontal heterogeneities common to mixed marine-continental traces is a possible reason of additional noise and complication of Green function waveforms emerging from these NCFs.

Stacking daily cross-correlations for each month of a year for several years of observations is a way to study their seasonal variations in details. Unlike Stehly et al. (2006) who used 15-day sliding stacking over a year, we had an opportunity to stack 60–90 daily cross-correlations for a month using 2–3 years of observations, thus essentially increasing the stability and SNR of emerged wavelets. Results of such stacking for all pairs of stations show that waveforms emerging at positive and negative correlation times vary regularly with season and independently one from another in all frequency sub-bands, most clearly for 2–5, 5–10, and 10–20 s.

Figure 3 presents such stacking that is made for stations AMZI and HRFI. At short periods (2–5 s), during the whole year with maximum in the Northern Hemisphere winter, the amplitude of the causal part of the cross-correlation is larger than that of the anticausal part, which is feebly

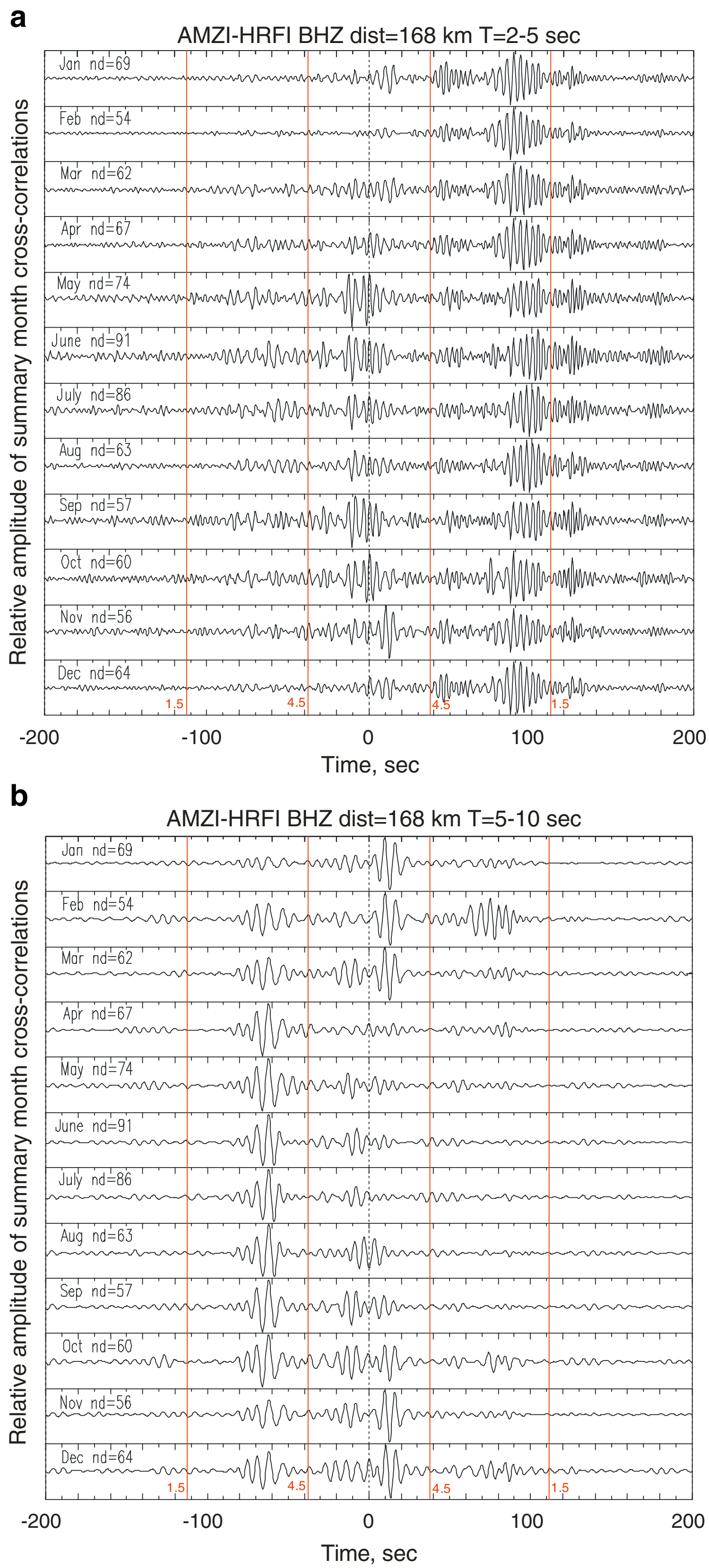

Fig. 3 The same cross-correlation as in Fig. 2a but stacked per months (every month includes more than 30 days collected from a few years of observation; this number of days is shown leftward in each panel) and filtered into three sub-bands, 2–5 s (**a**), 5–10 s (**b**), and 10–20 s (**c**). Amplitudes for every month are normalized to their maximum value. *Vertical red solid lines* indicate the signal windows corresponding to group velocities between 1.5 km/s and 4.5 km/s. The faster spreading signals outstripping Rayleigh waves and concentrating in the vicinity of cross-correlation zero time are considered as precursory noise

Fig. 3 continued

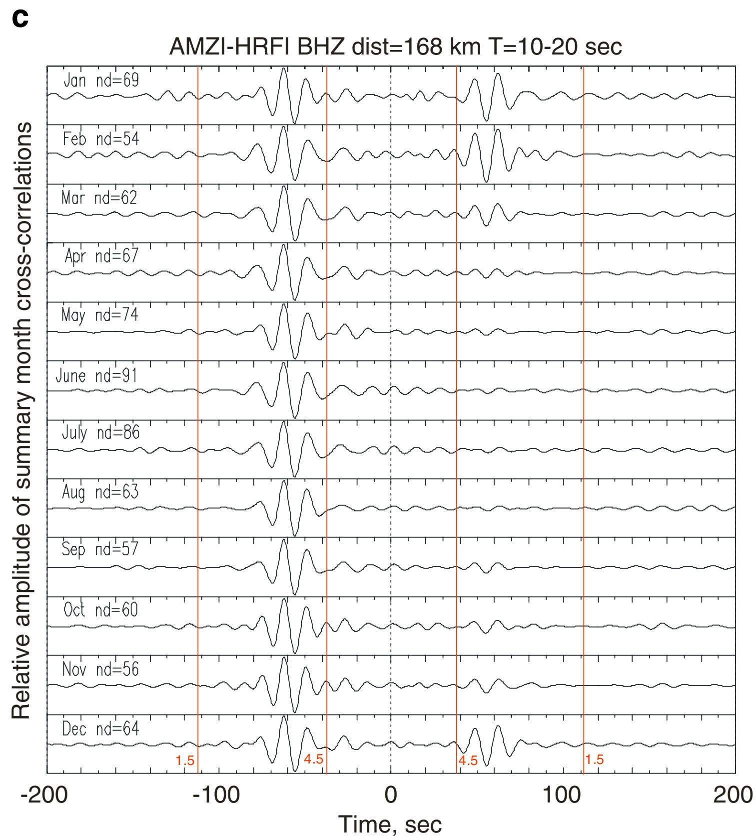

marked in summer and almost is lacking in other seasons (Fig. 3a). This indicates that most of the short-period noise Rayleigh wave energy propagates from north to south. On the contrary, in the other two sub-bands, 5–10 and 10–20 s, the opposite is observed. Namely, the noise is dominated by waves propagating from south to north during the whole year with maximum in the Northern Hemisphere summer, while the noise from the opposite northern direction activates only in the Northern Hemisphere winter months (Fig. 2b, c).

It is remarkable that at short periods 2–5 s and in the secondary microseism band 5–10 s, the vertical precursory noise gives symmetric salient arrivals outstripping Rayleigh waves traveling with the highest possible group velocity 4.5 km/s and concentrating mainly in the vicinity of cross-correlation zero time (Fig. 2). Because these precursory arrivals also show clear seasonal variability (Fig. 3a and b), they cannot be explained by influence of earthquakes not fully removed by temporal normalization (Bensen et al. 2007) and demand additional investigation.

3 Main types of seasonal variations

To present a seasonal variability of cross correlations' signals in a visual and vivid manner, we plot maximal amplitudes of signals against months in the seasonal diagram in the form of a year dial divided into 12 parts. The amplitude of a monthly cross correlation's signal is measured as maximal peak to peak in a time window corresponding to the Rayleigh wave group velocity range (1.5–4.5 km/s) and normalized firstly to 30 days observation period and then to the maximal among all 12 measured monthly amplitudes (name it the maximal seasonal amplitude). For the given pair of stations, we get thus two sets of 12 monthly amplitudes measured separately for causal and anticausal parts and corresponded to opposite

Fig. 4 Four types of seasonal diagrams showing relative variations of maximal amplitudes of NCF's signals depending on the month of a year, for primary ($T = 10$–20 s) and secondary ($T = 5$–10 s) microseisms. Monthly amplitudes in every diagram are normalized to 30-day observation period and to their relative maximum named here the maximal seasonal amplitude. Every pattern of seasonal diagrams corresponds to the ambient long-distance coherent noise coming to Israel from one of four different azimuth ranges (Table 1): **a** north-east type ($8° \leq az \leq 34°$), primary microseism; **b** north-west type ($az < 8°$; $az \geq 313°$), primary microseism; **c** north-east type, secondary microseism; **d** north-west type, secondary microseism; **e** south-east type ($132° \leq az < 176°$), primary microseism; **f** south-west type ($176° \leq az \leq 215°$), primary microseism; **g** south-east type, secondary microseism; **h** south-west type, secondary microseism

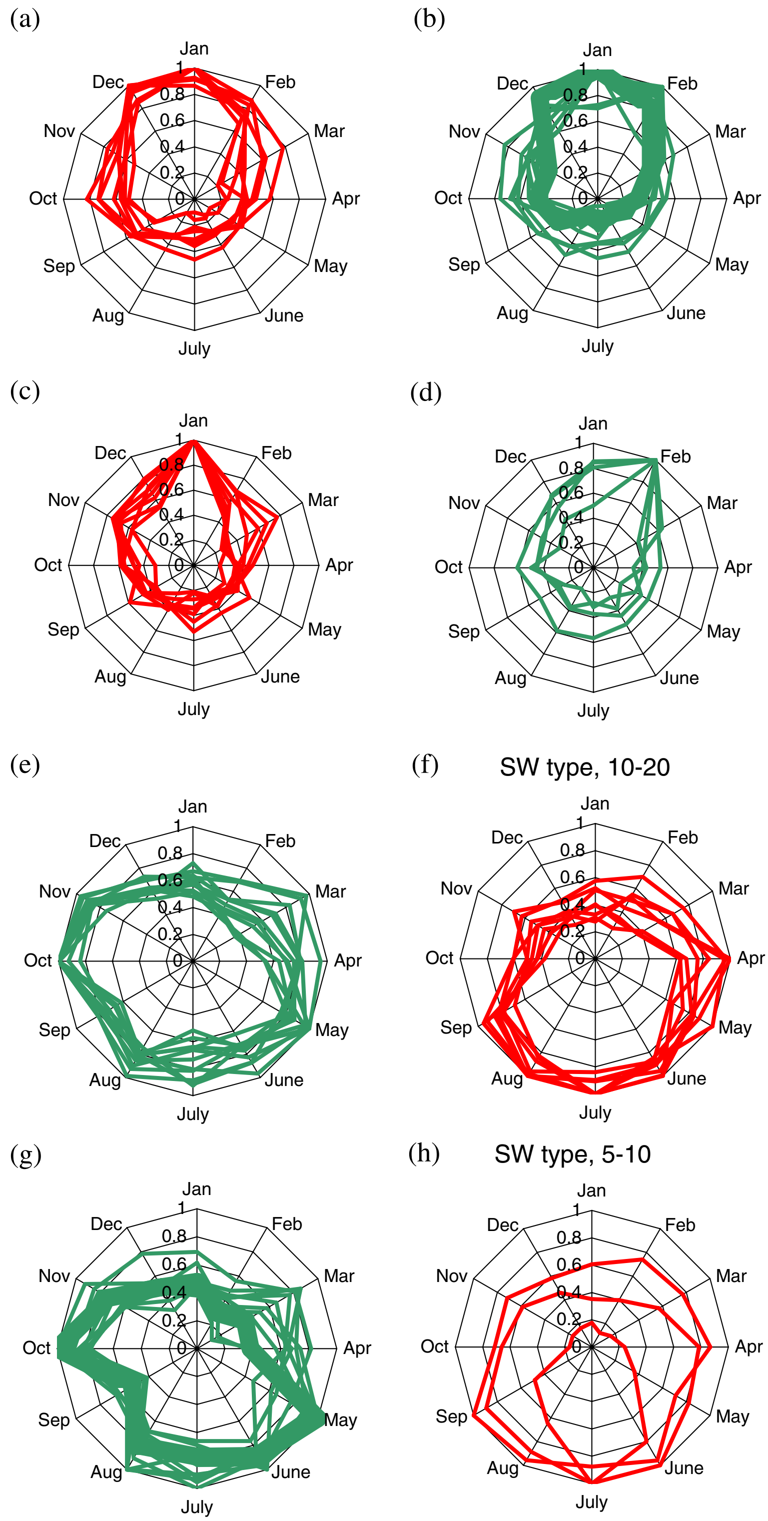

azimuths and numbers in Table 1 and, accordingly, to opposite directions of the coherent noise energy flux.

Grouping these measurements from all station pairs depending on their azimuth and analyzing their regularities, we reveal four typical seasonal diagrams for four azimuth ranges presenting the distribution of amplitudes with respect to the month of a year (Fig. 4, Table 1). These patterns are similar in the sub-bands 5–10 and 10–20 s, but for the former sub-band, we got less number of NCFs with a signal due to the aforementioned effect of obscuring the observation of the long-distance coherent wavefield by locally generated noise at island station CSS.

Two of these typical seasonal diagrams exhibit intensity variations during a year of the long-distance coherent noise arriving to the network from the northern directions (the north-east type and the north-west type). Both types show very low seismic noise level from spring to autumn, with essentially increasing amplitudes in the Northern Hemisphere winter. In the sub-band 10–20 s, the most active period is December–January for the north-east type (Fig. 4c), while for the north-west one, it begins 1 month later, in January–February (Fig. 4d). The azimuthal boundary between these two patterns is located at the meaning of about 8° that coincides with the direction of the grate circle arc passing through the stations MMLI and EIL (No. 1 in Fig. 5a and Table 1) and crossing the Novaya Zemlia islands and Arctic Ocean. For shorter periods between 5 and 10 s, seasonal diagrams are more strongly pronounced, giving sharp peaks of activity in January for the north-east type (Fig. 4c) and in February for the north-west type (Fig. 4d).

The other two typical seasonal diagrams correspond to the coherent noise coming from the southern directions (the south-east type and the south-west type, Figs. 4e–h and 5). Seasonal diagrams of both SE and SW types in the sub-band 10–20 s show minimal activity in the Northern Hemisphere winter, which in the case of primary microseism, is by a third less than the Northern Hemisphere summer activity for the south-east type (Fig. 4e) and is a third as great for the south-west type (Fig. 4f). On the other side, maximum amplitudes of long-distance coherent seismic noise are observed in May and October in the first case and since April to September with stable minimum in October in the second (Fig. 4e and f, respectively). Great circle trace passing through stations HRFI-AMZI (az = 176°, Table 1) presents the intermediate type of seasonal diagram (Fig. 5b, curve number −12). At periods between 5 and 10 s (Fig. 4g, h), all continental paths show mainly the same seasonal distribution of microseism activity as in the sub-band 10–20 s described above, but with slightly more pronounced peaks and troughs.

The four types of seasonal variation differ not only in the relative regularity of month activity over a year but also in the proportion of maximal seasonal amplitudes of cross correlations measured in four spectral sub-bands, depending on the azimuth (Fig. 6). These maximal seasonal amplitudes were used above for normalization of seasonal diagrams. For every pair of stations, we get two maximal seasonal amplitudes corresponding to opposite azimuths and numbers in Table 1. Moreover, they correspond to different or opposite seasons (winter for north directions and spring–summer–autumn for southern ones). They are normalized to 30 days of observation and corrected for geometrical spreading by multiplying the amplitude by the square root of the interstation distance. Due to insufficient knowledge of both attenuation coefficient as function of frequency and the local structure near the stations, we ignore the corresponding effects. This makes our amplitude estimates cruder probably within ±50% (Levshin et al. 2007).

In the 20–30 s band, maximal seasonal amplitudes remain relatively small and indifferent for all seasons and directions (Fig. 6). In contrast, amplitudes at shorter periods are essentially higher and vary in a wider range, supporting our division of seasonal diagrams into four types. Thus, the north-east (NE) type (Fig. 6a) is characterized as a whole by the low level of amplitudes in the 2–5 s band, while amplitudes in the bands 5–10 and 10–20 s are three to five times greater, with small prevalence of the latter. Similar distribution shows the diagram of south-west (SW) type, but amplitudes in the sub-bands 5–10 and 10–20 s are higher, with about twice prevalence of the latter (Fig. 6b).

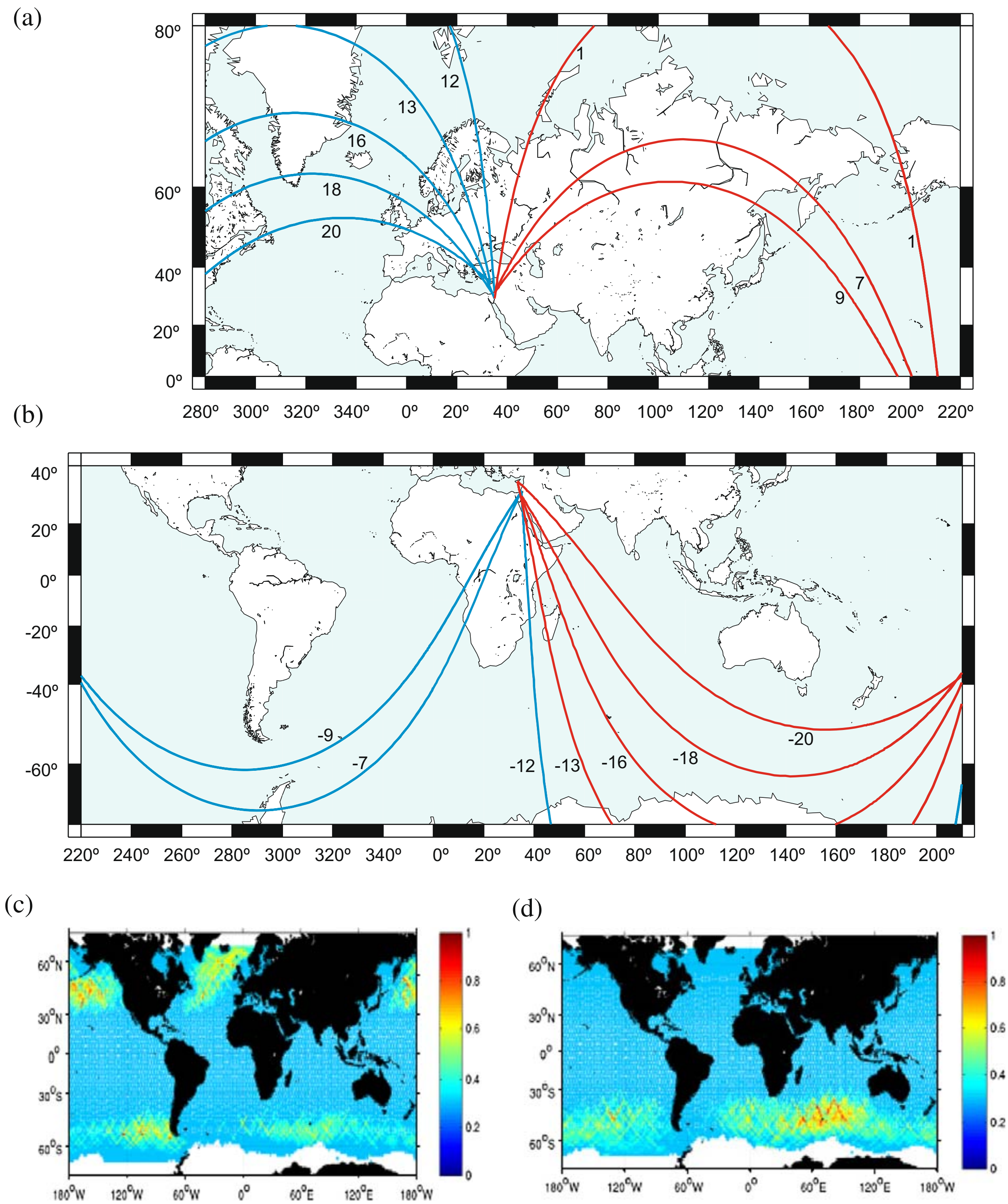

The north-west (NW) type (Fig. 6a), in the range of azimuths 338–360° (or −22–0°), has notably increased amplitudes of the 2–5 s sub-band observed on continental traces against a background of degradation of the 5–10 and 10–20 s components. And finally, amplitudes of the south-

Fig. 5 Great circle arcs passing through the pairs of Israeli stations and corresponding to the north (**a**) and south (**b**) directions of coming to Israel long-distance seismic coherent noise are compared to the global distribution of the square of wave height (normalized to the maximal value) measured by TOPEX/Poseidon during the winter (**c**) and the summer (**d**) of 1995 (http://sealevel.jpl.nasa.gov). All arcs are numbered in correspondence with Table 1. The MMLI-EIL (No. 1) and HRFI-AMZI (No. −12) arcs are boundaries between NE–NW and SE–SW types of seasonal variations, respectively. *Blue lines* correspond to the NW and SW types; *red* ones, to NE and SE types

east (SE) type (Fig. 6b) change from the minimal level for azimuths 158–170° to peak values for az = 147° (HRFI-KZIT, No. −18 in Table 1), with about quintuple amplification.

It is indicative that within the range of azimuths 180–215° (corresponding to the SW type), amplitudes of the month cross-correlations of primary and secondary microseisms vary in concord (Fig. 6b) that probably implies common origin of their long-distance coherent components. Very often, this concord is observed for all three frequency bands under consideration as in the following examples chosen for two pairs of stations located in southern and central parts of Israel (Fig. 7). These diagrams represent comparison of seasonal variations of maximal NCF Rayleigh wave amplitudes, normalized to 30 days of observation, and corrected as in Fig. 6 for geometrical spreading. The first pair of stations AMZI and HRFI (No. 12, az = 356°; No. −12, az = 176°) has the anomaly high-amplitude pick in Feb of the short-period (2–5 s) north noise (Fig. 7a, NW type) and amplitudes transitional between SE and SW types of seasonal variations for southern noise (Fig. 7b). The second pair MMLI and AMZI (No. 7, az = 26°; No. −7, az = 206°) presents the

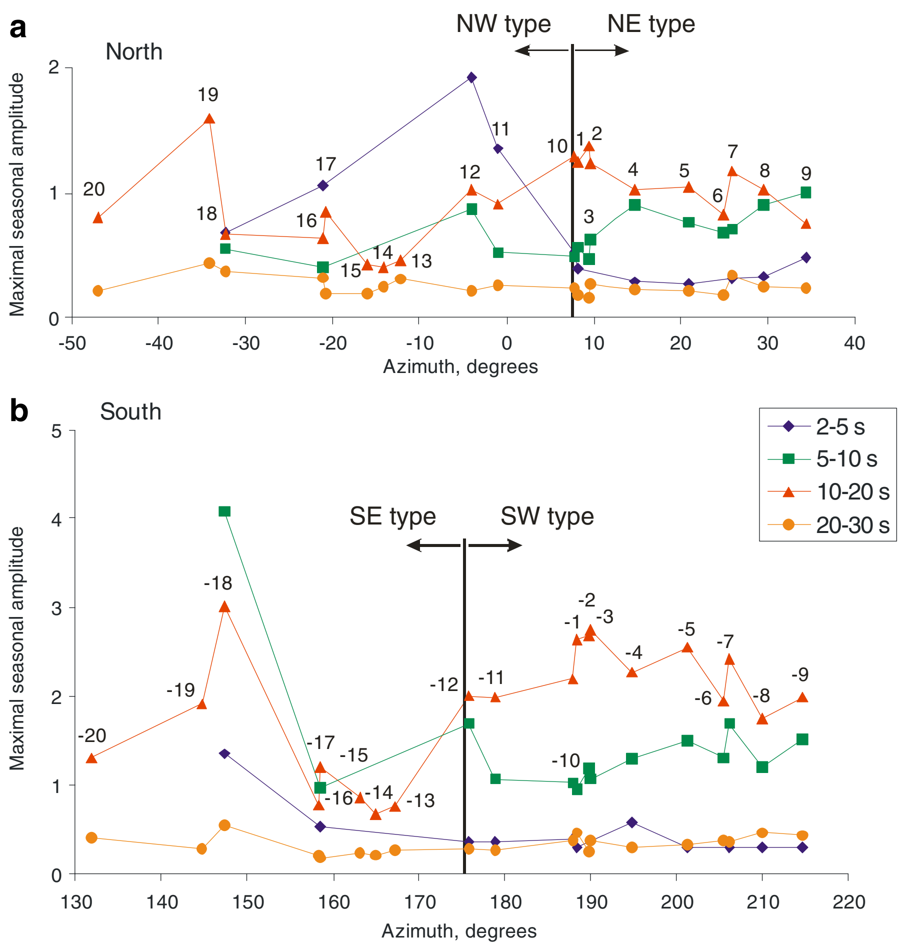

Fig. 6 Distribution of maximal seasonal amplitudes of cross correlations in great circle azimuth corresponding to couples of stations for the northern (**a**) and southern (**b**) seismic noise, in four spectral band-passes (2–5, 5–10, 10–20, and 20–30 s; *blue*, *green*, *red*, and *orange lines*, respectively). For every oriented pair of stations, the maximal seasonal amplitude is chosen as maximal among 12 peak to peak amplitudes of Rayleigh waves at 12 monthly NCFs. It is normalized to 30 days of observation and corrected for geometrical spreading. *Numbers* indicated are equivalent to the numbers of pairs of stations listed in Table 1. Opposite numbers correspond to opposite directions of coming of coherent noise

typical cases of the NE (Fig. 7c) and SW patterns (Fig. 7d). Diagrams in Fig. 7 show synchronous seasonal variations of amplitudes in the three sub-bands.

The other example (Fig. 8a) shows the case of anomaly high difference in maximal NCF amplitudes calculated for the northern and southern primary 10–20 s and secondary 5–10 s microseisms at pair of stations KZIT and HRFI. While for the north-west NW direction of the noise arrival (No. 18, az = 328°) the Rayleigh waveforms just hardly emerged during winter months, the noise from the opposite south-east direction (No. −18, az = 147°) gives the strongest for our network pick in July with the predominant secondary coherent microseism constituent. For comparison, other pair of stations with the close configuration KZIT and EIL gives three to four times less amplitudes of the south-east primary and secondary microseism arrivals (No. −16, az = 159°) corresponding to the standard SE type (Fig. 8d). For the north-west NW noise (No. 16, az = 339°) at the same couple

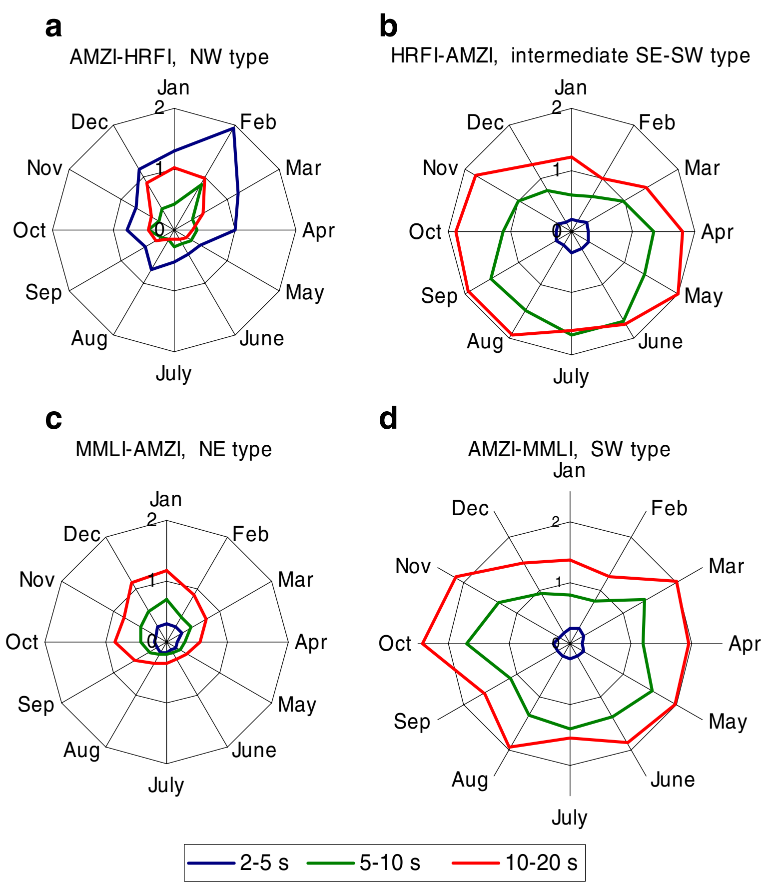

Fig. 7 Comparison of seasonal variation diagrams of maximal amplitudes of monthly NCF's signals, normalized to 30 days of observation and corrected for geometrical spreading, calculated for two pairs of stations located in southern and central parts of Israel, in three spectral sub-bands (2–5, 5–10, and 10–20 s; *blue*, *green*, and *red lines*, respectively). **a** Diagram for the northern noise at stations AMZI-HRFI (No. 12, az = 356°) corresponding to the north-west pattern of seasonal variations and having anomaly high short-period (2–5 s) amplitude in February. **b** Diagram for the same pair but in the reverse order (No. −12, az = 176°) for the southern noise. The form of this diagram is transitional between south-east and south-west types of seasonal variations. **c** Diagram for the northern noise at stations MMLI-AMZI (No. 7, az = 26°) being the typical representative of the north-east pattern. **d** Diagram for the same pair but in the reverse order (No. −7, az = 206°) for the southern noise. The form of this diagram is usual for its south-west pattern

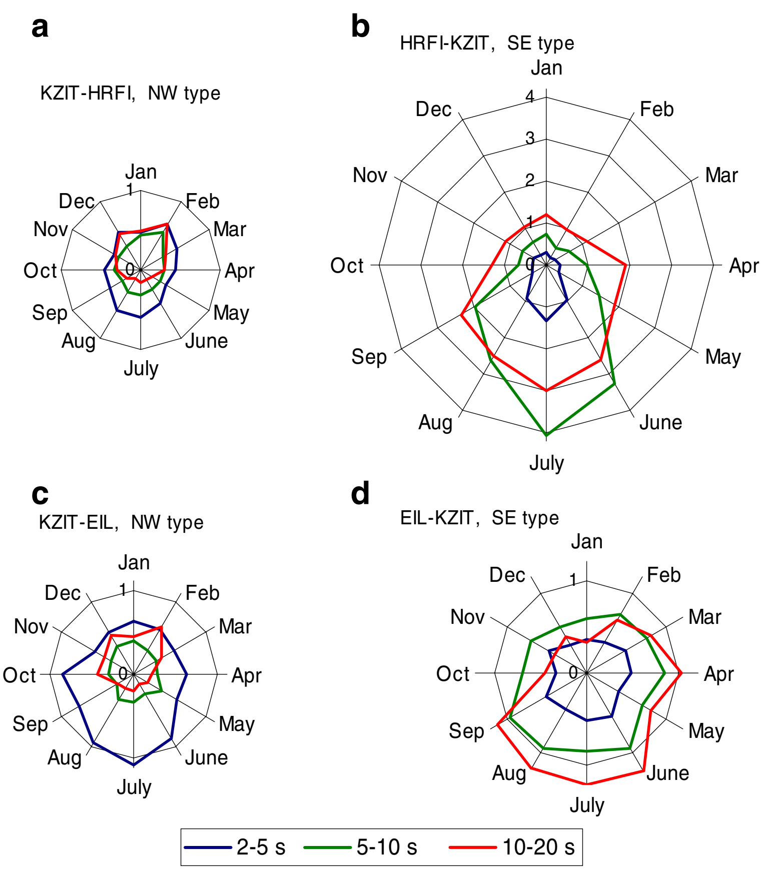

Fig. 8 The same as in Fig. 7 but for two pairs of stations located in southern part of Israel. **a** Diagram for the northern noise at stations KZIT-HRFI (No. 18, az = 328°). **b** Diagram for the same pair but in the reverse order (No. −18, az = 147°) for the southern noise. The couple of stations KZIT and HRFI demonstrate the north-west and south-east patterns of seasonal variations for all three sub-bands simultaneously. **c** Diagram for the northern noise at stations KZIT-EIL (No. 16, az = 339°). Short-period noise (2–5 s) has here the different pattern of seasonal variation than the NW type (Fig. 4b). **d** Diagram for the same pair but in reverse order (No. −16, az = 159°) for the southern noise (south-east type)

of stations and in the same sub-bands, amplitudes are still smaller (Fig. 8c), so their measurement becomes unreliable.

Amplitudes calculated for the short-period 2–5 s northern noise at these pairs of stations show the pattern different from the NW type that could be expected for this direction (Fig. 8a and c). It does not vary in concord with primary and secondary microseisms any more, at least in the summer period that is characterized by the increasing activity, particularly expressed at KZIT-EIL stations that may be explained by the influence of additional source of short-period coherent seismic noise to the north from these pairs of stations during the Northern Hemisphere summer.

4 Conclusion and discussion

As a whole, at the Israel–Cyprus Seismograph Network, the coherent long-distance noise from southern directions is predominant over that from northern directions at periods between 5 and 30 s, while the shorter period 2–5 s coherent noise comes mainly from the northern directions. This conclusion yields from the one-sided form of long-term cross correlations in the sub-bands and is congruent to the spectral shift toward long periods for the southern noise relative the northern one (Fig. 2).

Concord observed for the seasonal diagrams in the sub-bands 2–5, 5–10, and 10–20 s suggests that corresponding to them microseism have a common long-distance origin within every four ranges of azimuth (Table 1). Seismic noise coming to Israel from these four directions is generated in the areas of North Atlantic (NW type), North Pacific (NE type), South Atlantic (SW type), Indian Ocean, and South Pacific (SE type). This inference does not coincide with the global conclusion made by Stehly et al. (2006) about the different nature of primary and secondary microseisms that probably is not as universal as these researchers assume. The difference between our data processing techniques is not likely a reason of different results; we firstly do temporal and spectral whitening, calculate broadband normalized cross-correlations (2–80 s), and then analyze them in different frequency windows, while Stehly et al. (2006) firstly filter raw data in two narrow frequency bands (5–10 and 10–20 Hz), make only temporal one-bit normalization for every filtered row separately, and afterward calculate cross-correlations. But it was shown by Bensen et al. (2007) that one-bit normalization is the particular case of the running-absolute-mean normalization that we apply and that both methods give similar cross-correlation waveforms. On the other hand, spectral whitening that we apply change spectral amplitude relation between different frequency bands of input data and resulting cross-correlations, but it is not important because Stehly et al. (2006) work with narrow frequency bands independently. Besides, spectral whitening do not affect on phase spectral components of data, and thus do not influence on a degree of symmetry of a resulting cross-correlation in different frequency bands that we use as the measure of the energy flux ratio of the waves traveling between stations in opposite directions.

Seasonal variations brightly expressed by diagrams in Figs. 4, 7, and 8 reveal weather changes over a year in the mentioned areas reflecting variations in the storms' intensity and ocean wave activity, most probably, in deep water regions. This meets conclusions made by Kedar et al. (2008) about the microseism origin in the open ocean. The argument we have is that the highest amplitude of cross correlations, which is observed in July, the middle of the Southern Hemisphere winter, corresponds to the HRFI-KZIT great circle arc passing through the southern parts of the Indian Ocean and Pacific far away from coastlines.

On the other hand, the frequent presence in the estimated from NCFs Rayleigh wave Green function of the low-period 2–5 s component, quickly attenuating with distance, may suggest conclusion made by Rhie and Romanowicz (2006) and supported by Yang and Ritzwoller (2008) that ocean wave energy is coupled to the solid earth predominantly near coastlines.

There is yet no reasonable explanation to the found contradictions, which could be solved however via additional cross-correlation studies and multi-disciplinary all-seasonal world ocean observations both on the surface and the bottom.

Acknowledgements This work was supported financially by the United States–Israel Binational Science Foundation. The authors would like to thank their American collaborators from the University of Colorado at Boulder, Prof. A. Levshin, and Prof. M. Ritzwoller for their attention and helpful discussions.

References

Bensen GD, Ritzwoller MH, Barmin MP, Levshin AL, Lin F, Moschetti MP, et al (2007) Processing seismic ambient noise data to obtain reliable broad-band surface wave dispersion measurements. Geophys J Int 169:1239–1260. doi:10.1111/j.1365-246X.2007.03374.x

Lin FC, Ritzwoller MH, Shapiro NM (2006) Is ambient noise tomography across ocean basins possible? Geophys Res Let 33:L14304

Gutenberg B (1951) Observation and theory of microseisms. In: Malone TF (ed) Compendium of meteorology. Am Meteorol Soc, Providence, pp 1303–1311

Kedar S, Longuet-Higgins M, Webb F, Graham N, Clayton R, Jones C (2008) The origin of deep ocean microseisms in the North Atlantic Ocean. Proc R Soc A 2091:777–893, March. doi:10.1098/rspa.2007.0277

Levshin AL, Barmin MP, Yang X, Ritzwoller MH, Randall GE (2007) Toward a Rayleigh wave attenuation model for Central Asia and surrounding regions. In: Proceedings of the 29th monitoring research review of ground-based nuclear explosion monitoring technologies, p 10. Denver, CO, 25–27 September 2007

Longuet-Higgins M (1950) A theory of the origin of microseisms. Philos Trans R Soc Lond 243:137–171

Paul A, Campillo M, Margerin L, Larose E, Derode A (2005) Empirical synthesis of time-asymmetrical Green functions from the correlation of coda waves. J Geophys Res 110:B08302.1–B08302.13. doi:10.1029/2004JB003521

Peterson J (1993) Observations and modeling of seismic background noise. U.S. Geol. Surv. Open File Rep. 93–322

Rhie J, Romanowicz B (2006) A study of the relation between ocean storms and the Earth's hum. Geochem Geophys Geosyst 7:Q10004. doi:10.1029/2006GC001274

Sabra KG, Gerstoft P, Roux P, Kuperman WA, Fehler MC (2005a) Extracting time-domain Green's function estimates from ambient seismic noise. Geophys Res Lett 32:L03310. doi:10.1029/2004GL021862

Sabra KG, Gerstoft P, Roux P, Kuperman WA, Fehler MC (2005b) Surface wave tomography from microseisms in Southern California. Geophys Res Lett 32:L14311. doi:1029/2005GL023155

Shapiro NM, Campillo M (2004) Emergence of broadband Rayleigh waves from correlations of the ambient seismic noise. Geophys Res Lett 31:L07614. doi:10.1029/2004GL019491, p 23

Shapiro NM, Campillo M, Stehly L, Ritzwoller MH (2005) High resolution surface wave tomography from ambient seismic noise. Science 307:1615–1618. doi:10.1126/science.1108339

Snieder R (2004) Extracting the Green's function from the correlation of coda waves: a derivation based on stationary phase. Phys Rev E Stat Nonlin Soft Matter Phys 69:046610. doi:10.1103/PhysRevE.69.046610

Stehly L, Campillo M, Shapiro NM (2006) A study of the seismic noise from its long-range correlation properties. J Geophys Res 111:B10306, p 12

Wapenaar CPA (2004) Retrieving the elastodynamic Green's function of an arbitrary inhomegeneous medium by cross correlation. Phys Rev Lett 93:254301. doi:10.1103/PhysRevLett.93.254301

Weaver RL (2005) Information from seismic noise. Science 307:5715. doi:10.1126/science.1109834, 1568–1569

Yang Y, Ritzwoller M (2008) Characteristics of ambient seismic noise as a source for surface wave tomography. Geochem Geophys Geosyst 9:Q02008. doi:10.1029/2007GC001814

Yang Y, Ritzwoller M, Levshin A, Shapiro N (2007) Ambient noise Rayleigh wave tomography across Europe. Geophys J Int 168:259–274. doi:10.1111/j.1365-246X.2006.03203.x